[JGR: Planets]

Supporting Information for

[Entrainment and Dynamics of Ocean-derived Impurities within Europa's Ice Shell]

[J. J. Buffo[1,2], B. E. Schmidt[1], C. Huber[3], C. C. Walker[4]]

[[1]Georgia Institute of Technology [2]Dartmouth College [3]Brown University [4]Woods Hole Oceanographic Institution]

Contents of this file

Introduction

The following supporting information contains text and figures which provide additional context, detailed description, or visual aids to assist in the comprehension of the main manuscript.

S1 – Liquidus Curves for Putative Europan Ocean Chemistries

Crucial to the functionality of the model is the accurate simulation of the ocean/brine phase change, which is heavily dependent on the composition and concentration of the ocean/brine in question (Table 2). To accommodate the diverse array of proposed Europan ocean chemistries a software package was designed to calculate the concentration dependent liquidus curve for a given ocean/brine composition (Liquidus 1.0). The software utilizes the open source equilibrium chemistry code FREZCHEM (Version 6.2). A given aqueous solution is simulated at an array of temperatures and concentrations and the mole fraction of solid ice, under each condition, is tracked. For each concentration, the midpoint between the warmest temperature where any solid ice is present and the next warmest temperature is calculated. A quadratic fit is applied to these midpoints, and this is taken to be the liquidus curve for the solution. An example can be seen in Figure S3. Liquidus 1.0 and its associated documentation can be found at:

https://github.com/jbuffo/Liquidus-1.0/releases/tag/v1.0

S2 – Material Properties of Ice

Many of ice's material properties are thermally, chemically, and structurally dependent. Ice density is affected by temperature, porosity, and salt content [*Johnson et al.*, 2017a]. Its rheology is dependent on grain size, liquid fraction, and temperature [*Barr and McKinnon*, 2007] and its specific heat, thermal conductivity, and dielectric properties are all affected by local thermochemistry [*Kalousová et al.*, 2017; *Weeks and Ackley*, 1986]. As such, the properties and dynamics of Europa's ice shell will be dictated by these complex dependencies. This directly impacts buoyancy estimates, predicted ice shell thermodynamics, and the synthesis of future mission data [*Grima et al.*, 2016; *Johnson et al.*, 2017a; *McKinnon*, 1999; *Phillips and Pappalardo*, 2014]. A full foray into the implications of these dependencies on our current results is beyond the scope of this work, however the general applicability of the constitutive equations allows straightforward integration of more complex material properties, as demonstrated by the following example.

For ice, thermal conductivity is commonly described as varying inversely with temperature (e.g. Johnson et al. (2017) utilize the relationship $k = 651/T$ W/m, where k is thermal conductivity and T is temperature). An ice shell of thickness H, with ocean temperature T_{oc}, and surface temperature T_S, supports conductive equilibrium temperature profiles of the form:

$$T(z) = T_S \left(\frac{T_{oc}}{T_S}\right)^{z/H} \qquad (S1)$$

Where z is depth beneath the surface. The resulting thermal gradient at the ice-ocean interface and its dependence on ice shell thickness can be seen in Figure S6. Implementing an inverse relationship between thermal conductivity and temperature leads to amplified thermal gradients at the base of the ice shell. The constitutive equations relating bulk salinity to thermal gradient (Table 1) can then be utilized to investigate the resulting variance in ice shell composition induced by the modified thermal conductivity (Figure S6). At all depths an increase in bulk salinity is observed due to the amplified thermal gradients at the ice-ocean interface. These new bulk salinities will in turn increase near surface density values, alter electrical permittivity estimates, and affect predictions of other material properties. The overall salt content in the ice shell will increase by ~0.3%. This example demonstrates the versatility and applicability of the constitutive equations,

which can easily be implemented to account for the effects of impurities on a given ice shell process. Future work will utilize the current results (one-dimensional reactive transport model and constitutive equations) to investigate the effects of entrainment rate and ice composition on a broader class of geophysical processes, on a number of ice-ocean worlds, in greater detail.

S3 – Basal Fractures

To apply the model to basal fractures, we adapt the model by assuming the fractures have a characteristic basal width and penetration depth and altering the gravity drainage parameterization to account for the new geometry of the active layer (Figure S7). The fracture width and penetration depth are determined using a linear elastic fracture mechanics (LEFM) model. Fracture mechanics theory is based upon the assumption that all materials contain defects that affect their load-bearing capacity. LEFM, specifically, is a simplified approach that models the propagation of initial starter cracks or flaws in an elastic layer by assessing stress concentration near the crack tip. In reality, ice is not a linear elastic material, as its deformation is best described by a viscoelastic rheology. However, on short timescales such as that of fracture propagation, it behaves elastically. As such, LEFM is an adequate approximation to study fracture propagation in ice. It has been widely used in terrestrial ice systems to determine surface and basal fracture penetration depth (e.g., [*Van der Veen*, 1998a; b]), as well as in planetary surface fracture applications (e.g., [*Rudolph and Manga*, 2009]). Full details and analysis regarding the application to basal planetary fractures can be found in Walker et al., (in prep.); in essence, the height to which basal fractures propagate is controlled primarily by the tectonic stress field in which the fracture starts, overburden pressure at depth, and water pressure at the base. These stresses are additive at the crack tip, and the fracture propagates until this combined stress falls below the tensile strength of ice. We have conducted analyses using tensile strengths of 0 (no strength), 0.1 MPa $m^{1/2}$ and 0.4 MPa $m^{1/2}$ [*Rist et al.*, 1999]; at the depths of basal crevasses, the differences are very small, so we present the 0.1 MPa $m^{1/2}$ results here. For this application, we have assumed the base of the ice shell or ice lid is at hydrostatic equilibrium, i.e., basal water pressure is equal to the overburden pressure. We apply a range of tectonic (far-field) stresses to determine heights to which fractures propagate and their associated basal widths. Using these heights and widths, we produce simple basal fracture geometries; although fracture geometries are almost certainly more complex in reality, this simplified triangle ideal is also used in terrestrial studies (e.g., [*Luckman et al.*, 2012]).

New constitutive equations are produced for each fracture geometry and ocean/brine composition combination (an example can be seen in Figure S7). Three fracture scenarios have been simulated; an ice-ocean fracture due to a 0.1 MPa stress in a 25 km thick ice shell, an ice-ocean fracture due to a 2 MPa stress in a 25 km thick ice shell, and an ice-lens fracture subject to a 2 MPa stress in a 3 km ice lid. All scenarios assume the ambient ice shell formed from the Europan ocean chemistry of Table 2 with a concentration of 12.3 ppt. The ice-ocean simulations assume this same fluid fills the fractures and re-freezes. The ice-lens simulation assumes a 100 ppt fluid fills the fracture and re-freezes. This was done assuming the lens formed via eutectic melting, leading to a hypersaline chemistry. The fractures are assumed to freeze horizontally inward due to the thermal gradients produced by a conductive temperature profile for a 25 km thick shell with T_s=100K and T_{oc}=273K (i.e. the temperature difference between the ice shell at a given depth and the fluid infilling the fracture, divided by the horizontal thickness of ice formed in the fracture at that given depth).

S4 – Solidification Rates

To demonstrate the model's ability to produce solidification rates the longevity of the 2 MPa stress induced, ice-ocean interface, basal fracture is investigated. Implementing the geometry (Depth – 21.925 km, Width – 220.9 m) the multiphase reactive transport model is used to simulate the evolution of the fracture's ice-ocean interface. The spatiotemporal evolution of the freezing front can be seen in Figure S8. This process is carried out for a range of thermal gradients, and the associated solidification front propagation velocities can be obtained by:

$$v_m(t) = \dot{x}_m(t) \qquad (S2)$$

where v_m is the solidification front propagation velocity, and $\dot{x}_m$ is the time derivative of the solidification front position. The relationship between thermal gradient and ice-ocean interface propagation velocity can be seen in Figure S8. A linear fit, representing ice-ocean interface growth rate as a function of local thermal gradient, is produced (setting the y-intercept to zero, guaranteeing $v_m(t)$=0 for $\partial T/\partial z$=0 [See Figure S8]).

The relationship derived between solidification front propagation speed and local thermal gradients as well as the results from its application to a simulated basal fracture in a 25 km thick Europan ice shell agree with intuition. In regions with high thermal gradients (large undercooling) the solidification front propagates quickly, entraining larger amounts of impurities in the ice. Conversely, in regions with lower thermal gradients the freezing front propagates more slowly, allowing for expulsion of impurities out of the ice, and into the underlying/adjacent ocean. This results in the rapid solidification of the upper and edge regions of the fracture, where high bulk salinities can be seen. Meanwhile, in the lower portion of the fracture a longer-lived remnant of the fracture slowly diminishes, forming nearly pure ice as it freezes out. Unfortunately, to our knowledge, there exists no detailed measurements of the thermochemical evolution of potential fracture refreeze analogs in the terrestrial cryosphere (e.g. solidification of sea ice leads, infilling and solidification of basal ice shelf fractures). However, the solidification of mafic dikes and binary metal alloys frequently display similar thermal gradient dependent compositional structures [*Chistyakova and Latypov*, 2010; *Martorano et al.*, 2011]. While this example of thermally driven fracture closure is undoubtedly an oversimplification, neglecting mechanics/movement of the ice shell, fluid flow within the fracture, evolving fracture geometry, and infilling of the fracture due to marine ice accretion, it demonstrates the model's capability of simulating these environments. As shown here, with small modifications the model can be applied to an array of hydrological features with diverse thermochemical properties, making it a useful tool in understanding the dynamics and evolution of ice-ocean worlds.

S5 – Solution Stability

There are two instances within the manuscript where outputs from the numerical model exhibit observable scatter, which may spark concern for the model's stability; immediately after the model is initiated at a given depth (e.g. Figure S4), and when the model is subject to high salinities and low thermal gradients (e.g. Figure 3). Here we discuss both instances and provide rationale for why the observed scatter is not indicative of instability within the model. First, throughout the manuscript, a small number of values (< 1m of simulated ice) produced immediately after the initiation of the model are excluded from plots and fit lines (e.g. Figure 3). It is shown that including these values minimally affects the resulting constitutive equations and fit lines (See 'All vals' vs. 'Filtered' fit lines of Figure 3). The cause for this scatter is the abrupt ice-ocean interface initial condition. At the beginning of each run at depth (i.e. 10m, 50m, 100m,

etc.) the domain is modeled as being entirely liquid and in contact with a solid overlying ice shell whose thermal gradient at the interface is governed by the conductive equilibrium assumption ($dT/dz = (T_S - T_{oc})/H$). The lack of a mushy layer at the interface at the onset of the simulation means that one has to form. Coupled with the rapid freezing caused by the suddenly undercooled boundary, nonlinear patterns in the resulting predicted bulk salinities arise (observed scatter). However, these nonlinearities quickly stabilize to a uniform solution regardless of the initial conditions implemented (See Figure S9). All four selected initial conditions produce predicted bulk salinity values which vary by less than 0.2% by the time 1m of ice has frozen. Thus, we conclude that the scatter observed at the onset of simulations is not indicative of instability within the model.

The second condition under which scatter in the model output is observed is when a highly saline ocean is subject to low thermal gradients (e.g. bottom row of Figure 3). The scatter in this regime can be attributed to the increased sensitivity of the model to changes in liquid fraction at high salinities. Many parameters in the model are dependent on pore fluid salinity and local porosity (e.g. melting temperature, gravity drainage parameterization, molecular diffusion). Additionally, some of these dependencies are nonlinear (e.g. melting temperature, molecular diffusion). As an example, consider a closed system with salinity S_1 and porosity ϕ_1. If this system freezes so as to have a new porosity, ϕ_2, the new salinity, assuming all salt is rejected from the forming ice, can be written $S_2 = (\phi_1/\phi_2)\, S_1$. Without loss of generality, let $(\phi_1/\phi_2) = 2$. In this case, the new salinity will always be double the original salinity. In low salinity systems (e.g. the 12.3 ppt Europan ocean) this results in a change in salinity of $\mathcal{O}(10)$, while in high salinity systems (e.g. the 282 ppt Europan ocean) this results in a change in salinity of $\mathcal{O}(100)$. While the iterative nature of the finite difference model includes preset tolerances for interdependent variables ($T = 0.01\ K, S = 0.01\ ppt, \phi = 0.001$), these accepted errors can propagate through the solutions differently. Namely, as shown above, higher salinity oceans and pore fluids are more sensitive to changes in porosity, which can in turn impact estimations of eutectic temperature, gravity drainage, and molecular diffusion. This trend in increased scatter with increased salinity can be seen in Figure 3 (12.3 ppt – no scatter, 100 ppt – some scatter, 282 ppt – most scatter). Importantly, it is demonstrated that the scatter minimally affects the predicted constitutive equations. This is supported in three ways; 1) there is minimal variation between fit lines which include the scattered data and fit lines which exclude the data (See 'Filtered Fitline' vs. 'Shallow Fitline' of the 'Total Salt vs. Depth (Zolotov 282ppt)' plot in Figure 3), 2) the average values of the scattered data (green stars of Figure 3) tend to lie near the lower end of the scattered data range, suggesting the majority of the simulated values do not suffer from scatter, 3) the limits of the predicted constitutive equations approach their theoretical lower limits at large depths and low thermal gradients ($S_{lim} = \phi_c S_{oc}$), as expected. Thus, we believe our derived constitutive equations are not appreciably affected by the observed scatter in the limit of high salinity and low thermal gradient, and that this scatter is a benign byproduct of error propagation within the finite difference model.

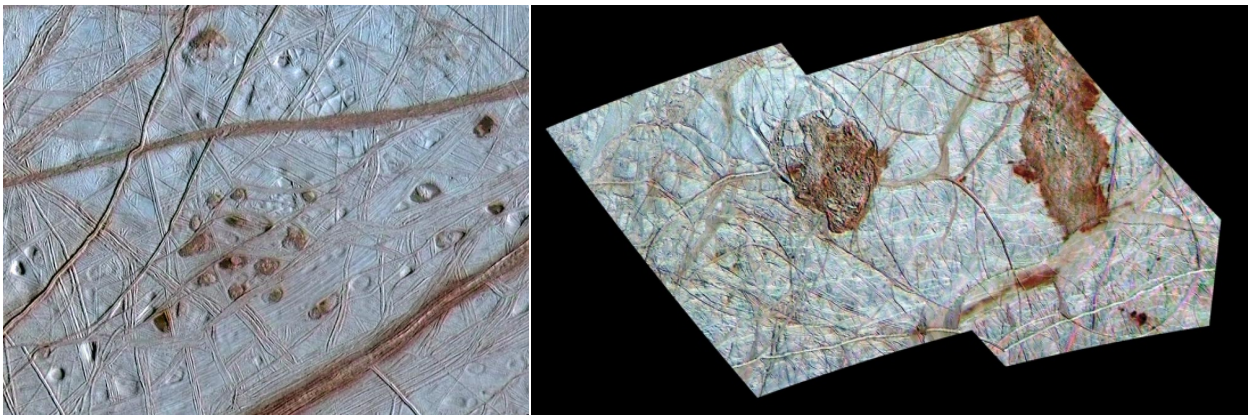

Figure S1 – Europa's geological features. Impurity rich geological features are found across the surface of Europa, indicated by their dark and red coloration. (Left) Dark red material associated with the most recently emplaced Lenticulae and Lineae (Image Credit: NASA/JPL/University of Arizona/University of Colorado – PIA03878) (Right) Similar concentrations of dark material is present at Thera and Thrace Macula, two regions of chaos terrain thought to be some of the most recently active regions on the moon (Image Credit: NASA/JPL/University of Arizona – PIA02099).

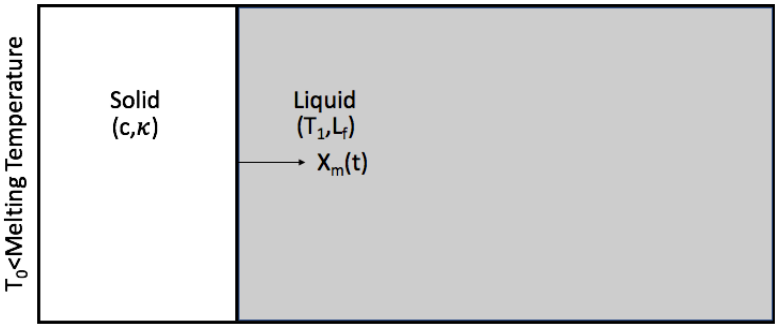

Figure S2 – The geometry and physical properties involved in the Stefan problem. The liquid at temperature T_1 loses heat through the solid whose left end is subject to a constant supercooling set to $T_0 < T_m$, leading to a propagating freezing front at position $x_m(t)$.

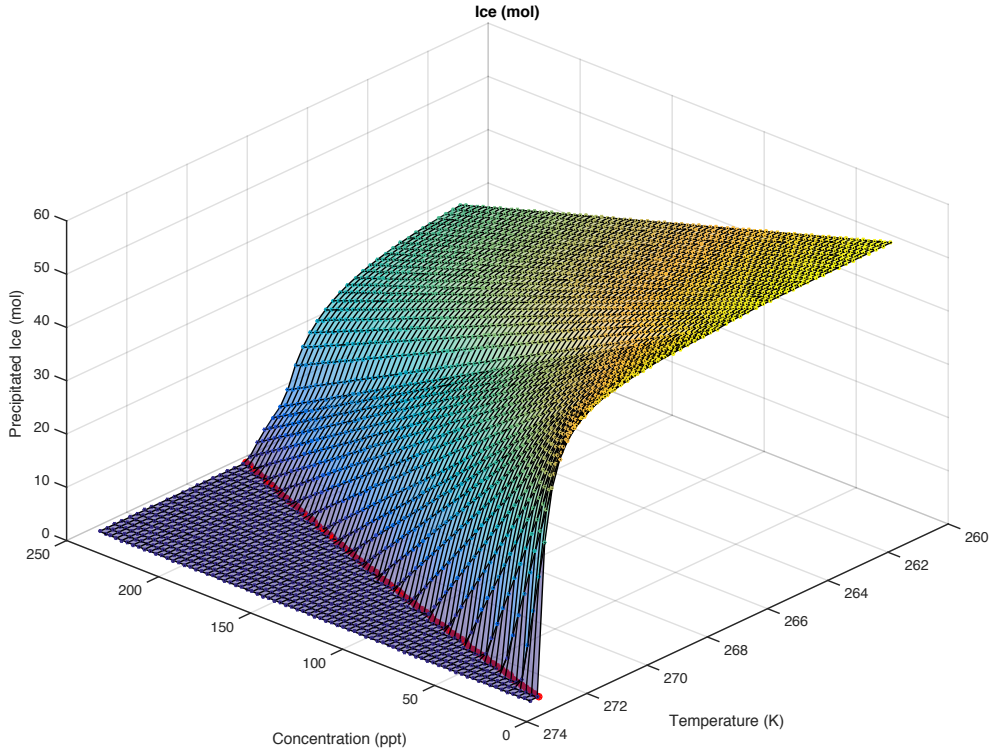

Figure S3 – Europan ocean liquidus. Temperature and concentration dependent ice precipitation for the Europan ocean chemistry of [*Mikhail Y Zolotov and Shock*, 2001]. Results produced using Liquidus 1.0. (Precipitated ice – gridded surface, quadratic fit liquidus curve – red line)

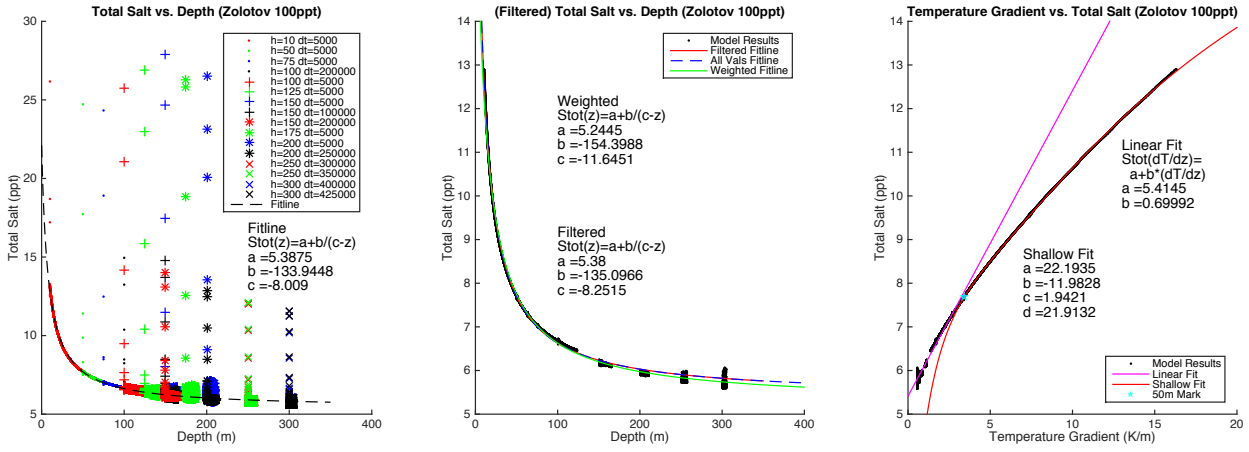

Figure S4 – Ice bulk salinity vs. depth and thermal gradient (100 ppt). Simulation results and constitutive equation fit lines for a hypothetical 100 ppt Europan ocean utilizing the chemistry given in Table 2. In addition to the two panels depicted for similar runs in the main text, a panel depicting the 'raw' simulation results is included. This includes values produced at the onset of simulations that contain some amount of scatter (See Supplementary Section S5 for details), as well as results for an array of temporal discretizations to investigate the effect this variance has on model output.

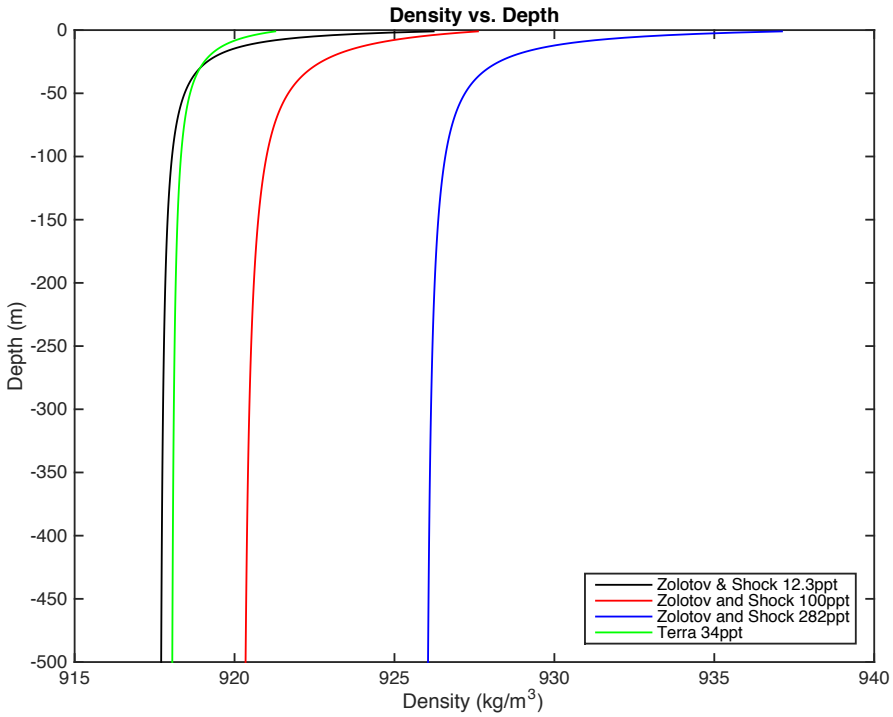

Figure S5 – Ice density vs. depth. Ice density variation with depth for the four ocean chemistries investigated. Depths greater than 500 m have been excluded as density variations below this point vary negligibly.

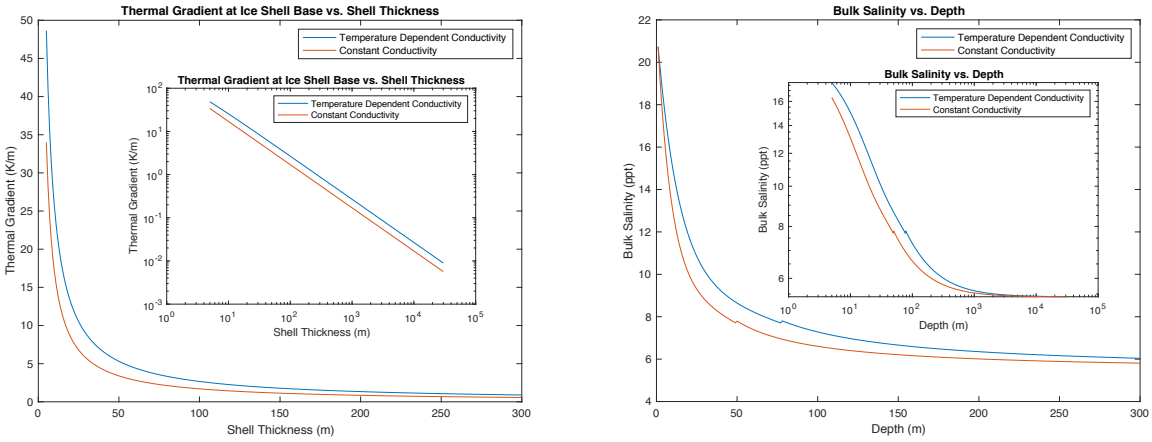

Figure S6 – Investigating the effects of temperature dependent thermal conductivity on impurity entrainment. (Left) Thermal gradients at the ice-ocean interface for a given ice shell thickness (5-300 m) utilizing a constant thermal conductivity (Red Line) and a thermal conductivity inversely related to ice temperature (Blue Line). Thermal gradients are calculated assuming equilibrium thermal states in the overlying ice, linear for constant thermal conductivity, and the thermal profile given by Equation S2 for the inversely dependent thermal conductivity. (Inset) Log-log plot of thermal gradient at ice-ocean interface vs. ice shell thickness for 5-30,000 m. (Right) The associated bulk salinity profiles calculated using the thermal gradients of the left plot and the constitutive equations of Table 3. (Inset) Log-log plot of bulk salinity vs. depth for 5-30,000 m. The slight jump is due to the transition between the linear and 'Shallow Fit Line' of Table 3.

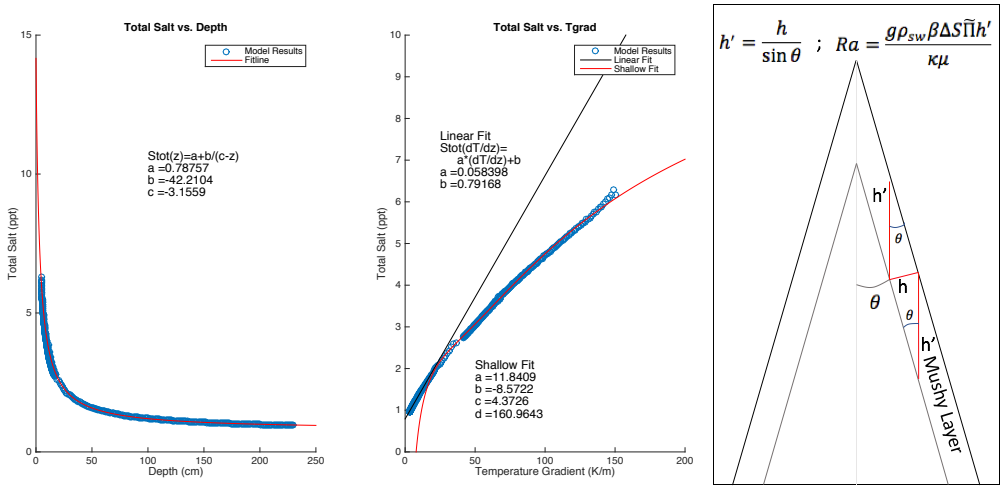

Figure S7 – Basal fracture geometry and constitutive relationships. (Left and Center) Model results (blue circles) and associated constitutive equations (red and black lines) for a hypothetical ice-ocean interface basal fracture (1.125 km penetration depth, 11.34 m basal width – associated with a 0.1 MPa stress). (Right) Basal fracture geometry, highlighting features that are used to modify the gravity drainage parameterization.

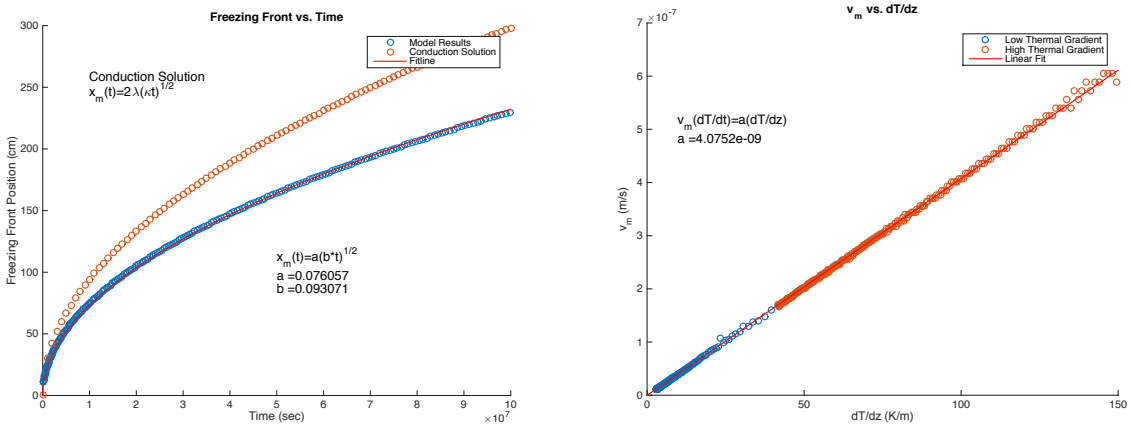

Figure S8 – Basal fracture ice-ocean interface evolution. Spatiotemporal evolution of the freezing front for a simulated basal fracture (Left) and the relationship between ice-ocean interface growth rate and local thermal gradient (Right) for a 12.3 ppt Europan ocean within a 0.1 MPa induced basal fracture (25 km ice shell). (Left - Conduction solution included to highlight the impact multiphase reactive transport processes have on ice-ocean interface dynamics)

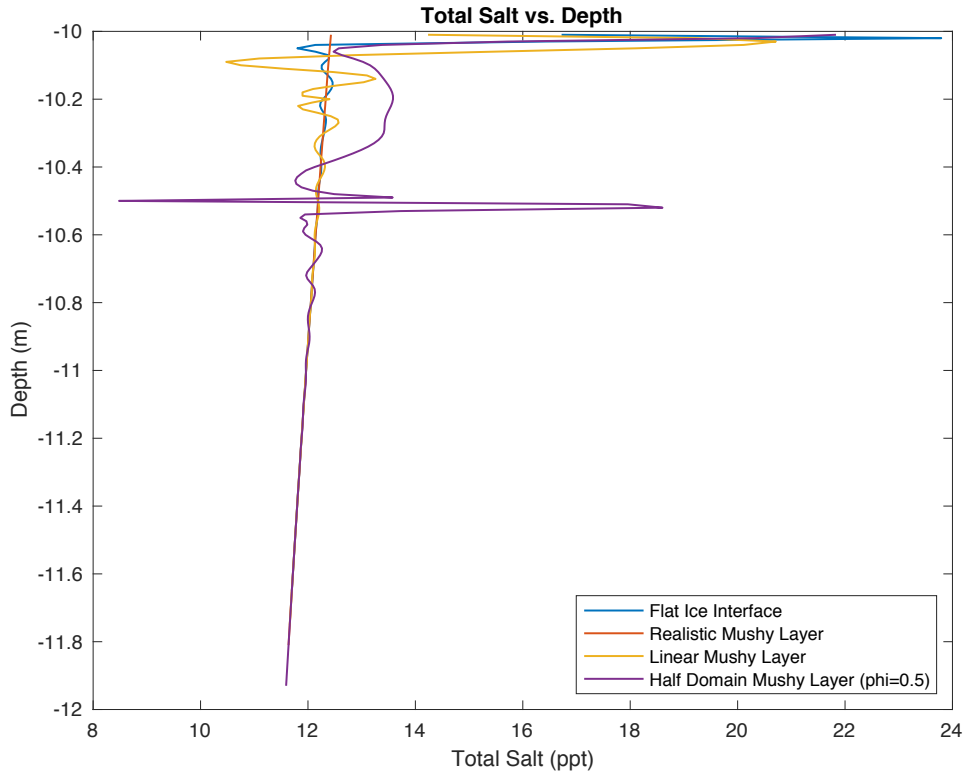

Figure S9 – Model stability under variable initial conditions (ICs). The predicted relationship between bulk salinity and ice shell depth for a 100 ppt Europan ocean when an array of disparate initial conditions is implemented, highlighting the collapse to a common solution. 'Flat Ice Interface' is the commonly used IC throughout the manuscript (no mushy layer, flat solid ice interface), 'Realistic Mushy Layer' utilizes the mushy layer properties (T, S, ϕ) present at 10m when the model is initiated at 9m as an IC, 'Linear Mushy Layer' utilizes a linear function of mushy layer properties ($T \in [269.30,271.31]\, K, S \in [100,200]\, ppt, \phi \in [0.05,1.00]$) over a 20 cm thick porous layer as an IC, 'Half Domain Mushy Layer' simulates the domain as being half mushy layer (50 cm) with a porosity of 0.5 and assumes the pore fluid has a salinity of 100 ppt as an IC.